



Research paper

Design and analytical model of a compact flexure mechanism for translational motion

Guangbo Hao^{a,*}, Xiuyun He^b, Shorya Awatar^c^a School of Engineering, University College Cork, Cork, Ireland^b Tyndall National Institute, University College Cork, Cork, Ireland^c Department of Mechanical Engineering, University of Michigan, Ann Arbor, MI, USA

ARTICLE INFO

Article history:

Received 6 May 2019

Revised 8 July 2019

Accepted 7 August 2019

ABSTRACT

This paper presents the design and analytical model of a compact flexure mechanism with a general beam shape, which can offer desirable single-axis translational motion capabilities. This design comprises two parallelogram flexure modules in a nested parallel arrangement and is termed the parallel double parallelogram flexure mechanism (or parallel-DPFM). Compared to the previously known parallel-DPFM, the proposed mechanism is more compact while offering several desirable performance characteristics including motion direction stiffness that is independent of bearing direction load, robustness against buckling, and suppression of error motion in the bearing direction. Closed-form planar force-displacement relations for the new design with a general beam shape have been derived to confirm these performance characteristics and provide design insights via parametric analysis. Nonlinear finite element analysis (FEA) and experimental testing are carried out to validate the analytically predicted performance characteristics for a specific beam shape that corresponds to the uniformly distributed-compliance case.

© 2019 Elsevier Ltd. All rights reserved.

1. Introduction

Flexure mechanisms provide finite motion along their degrees of freedom (DoF) via elastic deformation, and high stiffness (and therefore load bearing capability) along their degrees of constraint (DoC) [1–4]. In particular, beam-based flexure mechanisms achieve motion direction displacements from the bending of flexible beams, and load bearing capacity from the high axial stiffness of these beams [5]. However, such beam-based flexure mechanisms exhibit several inherent characteristics including dependence of motion direction stiffness on bearing direction load (i.e. load-dependence effect), parasitic error motion along the bearing direction, and degradation of bearing direction stiffness with the motion direction displacement [5–12]. These characteristics, which are generally undesirable, are the consequence of non-linearity in beam mechanics [6]. Load-dependence, mentioned above, can sometimes be useful when designing a mechanism with tuneable stiffness [10]. However, this load-dependence effect can be highly undesirable in many cases. For example, if the bearing direction is along gravity, then a variable payload will impact the motion direction stiffness and will make feedback or feedforward control very difficult in the motion direction.

The parallelogram flexure mechanism (PFM) (Fig. 1a) and the (serial) double parallelogram flexure mechanism (DPFM) (Fig. 1b) are two very common beam-based flexure designs that offer a single-axis translational DoF and compact footprint

* Corresponding author.

E-mail address: g.hao@ucc.ie (G. Hao).

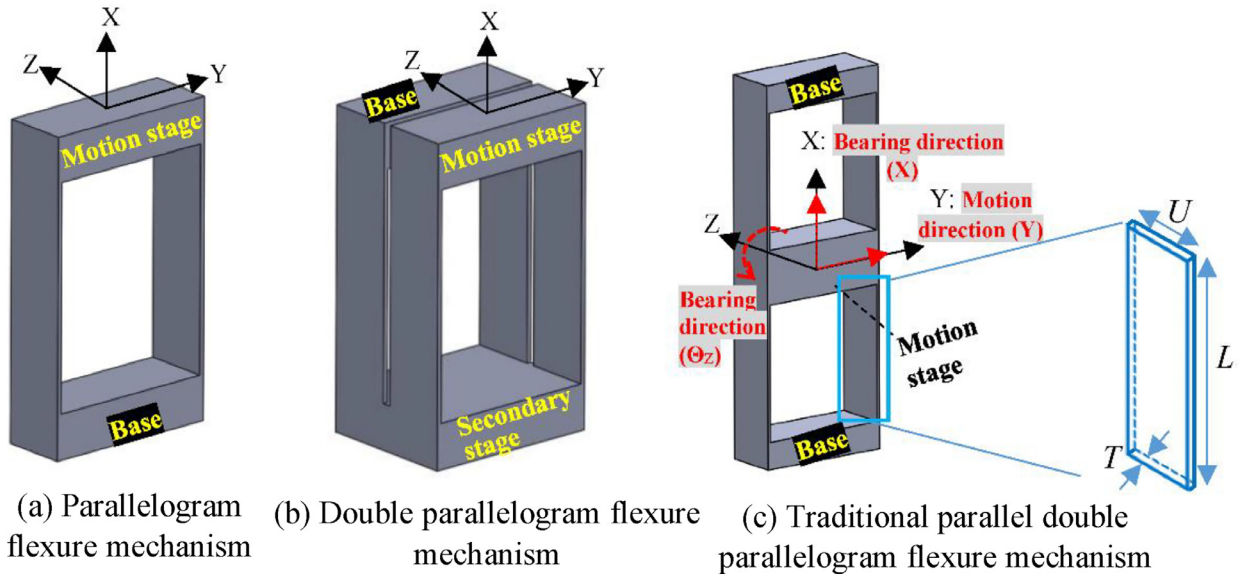


Fig. 1. Typical distributed compliance mechanisms considering planar deformation.

in various applications; and they are also used as building-blocks in more complex mechanisms [5,13,14]. A detailed review of these designs is provided in previous references [1,5,15]. The PFM suffers from parasitic error motion along the bearing (X and Θ_z) directions and dependence of motion (Y) direction stiffness on bearing (X) direction load. The DPFM comprises two PFMs reversely-connected in series [7] as shown in Fig. 1b, which results in various advantages over the PFM [5,7] such as reduced parasitic error motion and relatively lower dependence of motion direction stiffness on bearing direction load. Both designs are prone to buckling: the PFM buckles in the presence of high compressive bearing (X) direction load, and the DPFM buckles in the presence of high compressive as well as tensile bearing load. However, the greatest disadvantage of the DPFM is that the stiffness along the bearing direction sharply drops with displacement in the motion direction, which is the result of under-constrained secondary stage [6]. This under-constrained secondary stage also introduces additional undesirable dynamics [16,17].

In this paper, we present a compact parallel-DPFM, which comprises two PFMs connected in a nested and parallel layout. Traditional parallel-DPFM designs (as shown in Fig. 1c) that employ a symmetric layout of two identical PFMs are well-known in the literature [13,14] but are relatively less commonly used for large range of motion because of their over-constrained geometry [5–16]. The over-constraint results from the two PFMs in a symmetric layout (Fig. 1c): the X direction error motions of the two PFMs conflict each other, resulting in a nonlinear stiffness in the motion direction even in the absence of bearing (X) direction load [5]. However, this design ensures that the motion (Y) direction stiffness is insensitive to the bearing (X) direction load and buckling is largely avoided [16].

All these benefits and attributes of the traditional parallel-DPFM are carried over in the proposed nested parallel-DPFM design (Fig. 2). Most notably, this design is different from the traditional parallel-DPFM in that it offers a more compact, space-efficient geometry. Any bearing (X) direction load always appears in tension on one PFM and in compression on the other PFM, thereby avoiding zero stiffness in the motion direction (i.e. buckling condition). Since the motion direction stiffness of each constituent PFM is linearly dependent (to a high degree of approximation [6]) on the bearing direction load, the increase in stiffness of one PFM is negated by reduction in stiffness of the other PFM. This results in a design where the motion (Y) direction stiffness becomes largely independent of bearing (X) direction load. Like the PFM and the traditional parallel-DPFM, the nested parallel-DPFM has significantly less drop of bearing direction stiffness with motion direction displacement than the DPFM. Furthermore, the X direction parasitic error motion of one PFM is cancelled by the equal and opposite parasitic error motion of the other PFM. This does lead to over-constraint in the motion direction, limiting the range of motion, similar to the traditional parallel-DPFM. Given these various benefits of the proposed nested parallel-DPFM design that are qualitatively evident, the subsequent steps in this paper include quantifying these attributes via mathematical analytical modelling (note that an analytical model in this paper refers to the closed-form model presented in Section 2).

There are other interesting single-axis translational designs in the literature such as the DPFM with a slaving mechanism [17–19], which are more complex and do not have the desired characteristics including the load-independent motion direction stiffness and the robustness against buckling.

In summary, we present a variation of the parallel-DPFM in this paper (Fig. 2a) that is more compact than the traditional parallel-DPFM (Fig. 1c). In studying this flexure mechanism, we use a general beam shape for each flexure beam with one

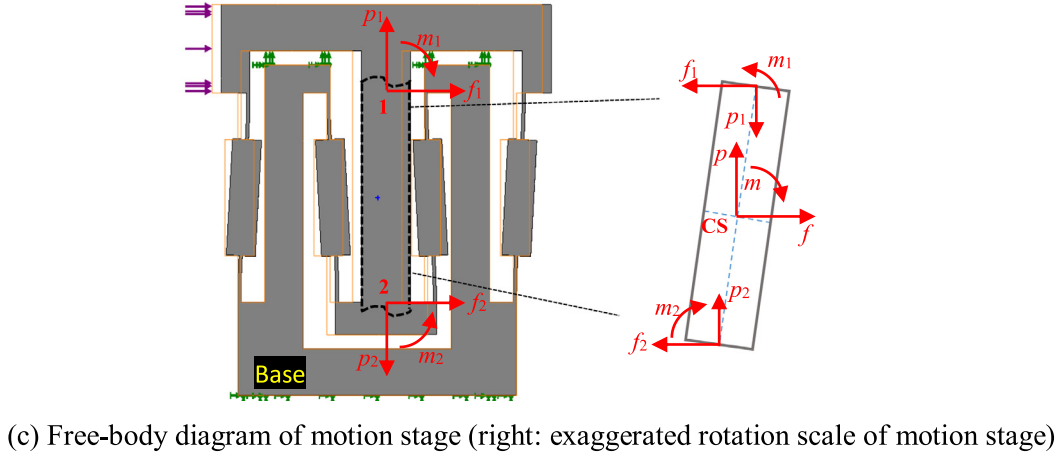
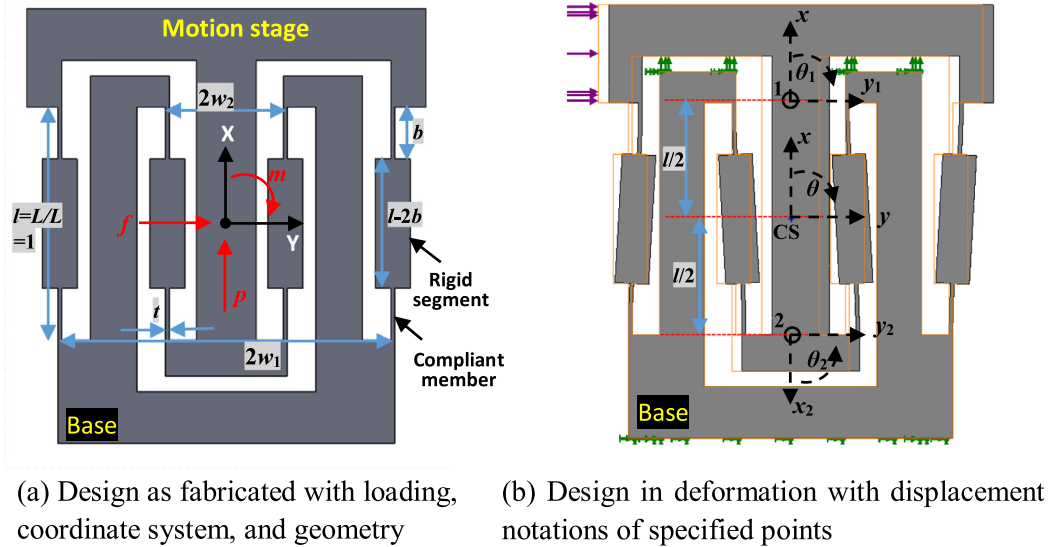


Fig. 2. The general parallel-DPFM with scalar parameters.

rigid middle segment and two compliant end-members. As expected, the range of motion in the motion (Y) direction is indeed limited for commonly used metals and stiff plastics due to the above described over-constraint, but this design nevertheless provides useful range of motion that is a few times the flexure beam thickness. This arrangement can be very valuable for applications where such a small stroke is adequate but insensitivity of motion direction stiffness to bearing direction load is critical [16].

As shown in Fig. 2b, there are three reference points of interest – 1, 2 and CS – on the motion stage, to define displacements and loads. Point CS refers to the location of the output displacements of the motion stage, and also to that of the applied external loads. A fixed coordinate frame (XYZ) is located at CS in the undeformed configuration of the mechanism. Normalisation is employed in the whole process of modelling in order to express all physical quantities and equations in a dimensionless/scalar format. Accordingly, all translational displacements and length parameters are normalized by the overall beam length L (the characteristic length), forces by EI/L^2 , and moments by EI/L . E denotes the Young's modulus of the material for an XY plane-stress condition and the plate modulus for an XY plane-strain condition. $I=UT^3/12$ denotes the second moment of cross-section area about the Z axis of the two compliant end-members of the beam, each with length B , thickness T , and depth U . Throughout the paper, all non-dimensional quantities are denoted by the corresponding lower-case letters with reference to Fig. 2. We use a scalar variable b ($= B/L$) ranging between 0 and 1/2 in this paper as a measure of the degree of distributed compliance of the general beam flexure, where $b=1/2$ means uniformly distributed compliance along each beam while $b \rightarrow 0$ corresponds to a lumped-compliance configuration. Since this paper uses the beam constraint model as the analytical modelling tool, the displacement range considered in the motion direction is limited to 10% of the beam length as justified in [5,6]. Although this range of motion may exceed the maximum practical displacement in designs

made of metals and stiff plastics, it would still be relevant for other commonly used softer materials such as polycarbonate and polypropylene [10,16] and rubber-like materials [20].

The remainder of the paper is organised as follows. Section 2 covers the closed-form/analytical models of the proposed flexure mechanism using general beams. These results are used in Section 3 to perform a theoretical parametric analysis of the characteristics of this flexure mechanism. Section 4 verifies the analytical model using nonlinear finite elements analysis (FEA). Experimental hardware setup and measurement results are presented in Sections 5 and 6, respectively. Conclusions are drawn in Section 7.

The primary contributions of this paper are summarized as follows:

- We present a parallel-DPFM design where the PFMs are configured in a parallel kinematic manner, nested one inside the other. The new design eliminates dependence of motion direction stiffness on bearing direction load, provides robustness against buckling, and suppresses motion in the bearing direction. While the parallel-DPFM is well known and studied in the literature [10,16] (Fig. 1c), the nested design is novel and offers the unique advantage of a compact footprint.
- We provide an analytical (closed-form) analysis of the flexure mechanism (assuming a general beam shape) that insightfully captures all the relevant non-linearities, and an FEA validation of this analysis. This analytical model captures the impact of the degree of distributed compliance on the various performance characteristics including nominal stiffness, stiffness variation, and error motions along the various directions in a parametric manner.
- Based on the closed-form analysis that relates the mechanism's dimensional parameters to its performance, we provide several insights to enable quick design. A set of dimensional parameters are selected for subsequent FEA and experimental validation.
- We present the careful design of a hardware setup to experimentally validate the above closed-form analysis, particularly the bearing load independent motion direction stiffness.

2. Closed-form modelling

The goal in this section is to formulate the relations between the input/external forces and the output displacements at the same point CS for the proposed general-beam parallel-DPFM (Fig. 2). We will employ the Beam Constraint Model (BCM) as developed and used in [5,6]. The BCM is based on the Euler beam model for slender beams and takes into consideration the geometric non-linearity associated with beam arc length conservation.

Parametric load-displacement equations of one parallelogram module (i.e., PFM), with respect to its local coordinate system at point 1 or 2 (Fig. 2c), can be obtained [6,21] as follows:

$$x_i = \frac{1}{2k_{33}} p_i - \frac{k_{11}^{(1)}}{2} y_i^2 - \frac{k_{11}^{(2)}}{2} p_i y_i^2 \quad (1a)$$

$$y_i = \frac{f_i}{2k_{11}^{(0)} + k_{11}^{(1)} p_i} \quad (1b)$$

$$\theta_i = \frac{1}{2w_i^2} (1/k_{33} - k_{11}^{(2)} y_i^2) [m_i - (2k_{12}^{(0)} + k_{12}^{(1)} p_i) y_i] \quad (1c)$$

where $i=1$ or 2 , which corresponds to the first or second parallelogram module (outer/inner one), respectively. The other symbols undefined above are the beam characteristic coefficients, which are the functions of b as explained in Appendix B [6]. Note that the assumption of small rotations has been made for the derivation of in Eq. (1).

Compatibility conditions between point 1 (or 2) and point CS are represented as below:

$$x_i = (-1)^{i-1} x - \theta^2/4 \quad (2a)$$

$$y_i = y + (-1)^{i-1} \theta/2 \quad (2b)$$

$$\theta_i = (-1)^{i-1} \theta \quad (2c)$$

where $i=1$ or 2 , representing the outer parallelogram or the inner parallelogram.

We can derive the load-equilibrium conditions among three reference points, 1, 2 and CS, based on Fig. 2c:

$$f_1 + f_2 = f \quad (3a)$$

$$p_1 - p_2 = p \quad (3b)$$

$$m_1 - m_2 + (f_1 - f_2)/2 - (p_1 + p_2)/2 = m \quad (3c)$$

There are 18 variables involved in the above 15 equations (Eqs. 1a–3c). Given any three of them, these equations can always be solved numerically. However, it is still very challenging to obtain analytical closed-form solutions even using commercial symbolic software such as Maple/Mathematica. It is desirable to obtain analytical (closed-form) solutions, which enable parametric design insight even though their accuracy might be limited by the range of loads and displacements. In this paper, certain approximations and strategies are used to obtain such closed-form solutions, as detailed below.

Firstly, we neglect the rotational contributions in the two translational compatibility conditions (Eqs. 2a and 2b), which reduce to

$$x_i \approx (-1)^{i-1} x \quad (4a)$$

$$y_i \approx y \quad (4b)$$

Note that the above simplification is appropriate as used in [5] since the rotational angle about the Z direction in the mechanism is usually two orders of magnitude smaller than the normalized Y direction translation, and the square of the rotational angle has a negligible contribution to the X direction translation. The FEA verification later in this paper will show the rationality of this simplifying assumption.

Substituting Eqs. (4a) and (4b) into Eqs. (1a) and (1b), we can further obtain the following two equations:

$$-\left(\frac{1}{2k_{33}} p_2 - \frac{k_{11}^{(1)}}{2} y^2 - \frac{k_{11}^{(2)}}{2} p_2 y^2\right) = \frac{1}{2k_{33}} p_1 - \frac{k_{11}^{(1)}}{2} y^2 - \frac{k_{11}^{(2)}}{2} p_1 y^2 = x \quad (5a)$$

$$\frac{f_2}{2k_{11}^{(0)} + k_{11}^{(1)} p_2} = \frac{f_1}{2k_{11}^{(0)} + k_{11}^{(1)} p_1} = y \quad (5b)$$

Combining Eqs. (5a) and (5b) and Eqs. (3a) and (3b), we can solve for the four internal forces, p_1 , f_1 , p_2 , and f_2 :

$$p_1 = \frac{p}{2} + \frac{k_{11}^{(1)} y^2}{1/k_{33} - k_{11}^{(2)} y^2} \quad (6a)$$

$$f_1 = \frac{f}{2} \left[1 + \frac{k_{11}^{(1)} p}{4k_{11}^{(0)} + \frac{2(k_{11}^{(1)})^2 y^2}{1/k_{33} - k_{11}^{(2)} y^2}} \right] \quad (6b)$$

$$p_2 = -\frac{p}{2} + \frac{k_{11}^{(1)} y^2}{1/k_{33} - k_{11}^{(2)} y^2} \quad (6c)$$

$$f_2 = \frac{f}{2} \left[1 - \frac{k_{11}^{(1)} p}{4k_{11}^{(0)} + \frac{2(k_{11}^{(1)})^2 y^2}{1/k_{33} - k_{11}^{(2)} y^2}} \right] \quad (6d)$$

Eq. 5(b) can also be used to derive the following form:

$$f_1 + f_2 = [4k_{11}^{(0)} + k_{11}^{(1)}(p_1 + p_2)]y \quad (7)$$

Substituting Eqs. (6a)–(6d) into Eq. (7), the motion (Y) direction equation is firstly obtained:

$$y = \frac{f}{4k_{11}^{(0)} + \frac{2(k_{11}^{(1)})^2 y^2}{1/k_{33} - k_{11}^{(2)} y^2}} \quad (8)$$

Eq. (2a) leads to:

$$x_1 - x_2 = 2x \quad (9)$$

Substituting Eq. (1a) into Eq. (9), we have

$$\frac{p_1 - p_2}{2k_{33}} - \frac{k_{11}^{(1)}}{2} (y_1^2 - y_2^2) - \frac{k_{11}^{(2)}}{2} (p_1 y_1^2 - p_2 y_2^2) = 2x \quad (10)$$

Further substituting Eqs. (2b), (6a) and (6c) into Eq. (10), the X direction motion (one bearing direction) is then derived as:

$$x = \frac{1}{4k_{33}} p - \frac{k_{11}^{(1)}}{2(1 - k_{11}^{(2)} k_{33} y^2)} y \theta - \frac{k_{11}^{(2)}}{4} p y^2 \quad (11)$$

where the three terms on the right hand side represent the pure elastic effect, the pure kinematic effect, and the elasto-kinematic effect, respectively. Note that Eq. (2b) including the rotation contribution is used to obtain a more accurate X direction motion that is able to capture the kinematic effect.

The final step is to obtain the solution of the planar rotational angle about the Z direction. Using the result of Eq. (8), we simplify Eqs. (6b) and (6d), respectively, as below:

$$f_1 = \frac{1}{2}f + \frac{k_{11}^{(1)}}{2}py \quad (12a)$$

$$f_2 = \frac{1}{2}f - \frac{k_{11}^{(1)}}{2}py \quad (12b)$$

Substituting the results of Eqs. (12a) and (12b) into Eq. (3c), we can obtain

$$m_1 - m_2 + \frac{k_{11}^{(1)}}{2}py \approx m \quad (13)$$

where the rotational contribution on the load-equilibrium equation (Eq. (3c)) is neglected again due to the reason mentioned earlier [5].

Substituting Eq. (4b) into Eq. (1c), and using the compatibility condition in Eq. (2c), we have

$$\frac{[m_1 - (2k_{12}^{(0)} + k_{12}^{(1)}p_1)y]}{w_1^2} + \frac{[m_2 - (2k_{12}^{(0)} + k_{12}^{(1)}p_2)y]}{w_2^2} = 0 \quad (14)$$

Using Eqs. (13) and (14), the two internal moments, m_1 and m_2 , can be derived, with m_2 explicitly expressed below:

$$m_2 = \frac{(2k_{12}^{(0)} + k_{12}^{(1)}p_2)yw_1^2 + (2k_{12}^{(0)} + k_{12}^{(1)}p_1)yw_2^2 - (m - k_{11}^{(1)}py/2)w_2^2}{w_1^2 + w_2^2} \quad (15)$$

We substitute Eqs. (15), (6a), (6c), and (4b) into Eq. (1c) to derive the equation in another bearing direction: Θ_z direction as below:

$$\theta = -\theta_2 = \frac{1}{2(w_1^2 + w_2^2)}(1/k_{33} - k_{11}^{(2)}y^2)[m - (k_{11}^{(1)}/2 + k_{12}^{(1)})py] \quad (16)$$

It is noted that the translational analytical models Eqs. (8) and ((11)) are very similar to those of the traditional parallel-DPFM, but the rotational analytical model is different from that of the traditional parallel-DPFM due to the new compact design [16].

Rearranging Eqs. (11), (8), and (16), we have

$$p = \left[x + \frac{k_{11}^{(1)}}{2(1 - k_{11}^{(2)}k_{33}y^2)}y\theta \right] / \left(\frac{1}{4k_{33}} - \frac{k_{11}^{(2)}}{4}y^2 \right) \quad (17a)$$

$$f = y \left[4k_{11}^{(0)} + \frac{2(k_{11}^{(1)})^2y^2}{1/k_{33} - k_{11}^{(2)}y^2} \right] \quad (17b)$$

$$m = \left[\theta / \frac{(1/k_{33} - k_{11}^{(2)}y^2)}{2(w_1^2 + w_2^2)} \right] + (k_{11}^{(1)}/2 + k_{12}^{(1)})py \quad (17c)$$

The normalised stiffness equations in all directions (X, Y and Θ_z) are shown below by differentiating Eqs. (17a), (17b), and (17c):

$$\begin{cases} k_x = \frac{\partial p}{\partial x} = \frac{4}{1/k_{33} - k_{11}^{(2)}y^2} \\ k_y = \frac{\partial f}{\partial y} = 4k_{11}^{(0)} + \frac{6(k_{11}^{(1)})^2y^2}{1/k_{33} - k_{11}^{(2)}y^2} + \frac{4(k_{11}^{(1)})^2k_{11}^{(2)}y^4}{(1/k_{33} - k_{11}^{(2)}y^2)^2} \\ k_\theta = \frac{\partial m}{\partial \theta} = \frac{2(w_1^2 + w_2^2)}{1/k_{33} - k_{11}^{(2)}y^2} \end{cases} \quad (17d)$$

Up until this point, we have derived closed-form expressions for three displacements, x , y , and θ along with their stiffness expressions, assuming a general beam shape. Based on these results, we can conclude the following.

- (a) Eq. (8) shows that the motion (Y) direction displacement is only influenced by the force along the same axis, analytically confirming the elimination of load-dependent effects (as defined in the introduction). One can observe that only the geometrical parameters associated with the beam size and shape (i.e. t and b) influence the normalized motion direction load-displacement relation.

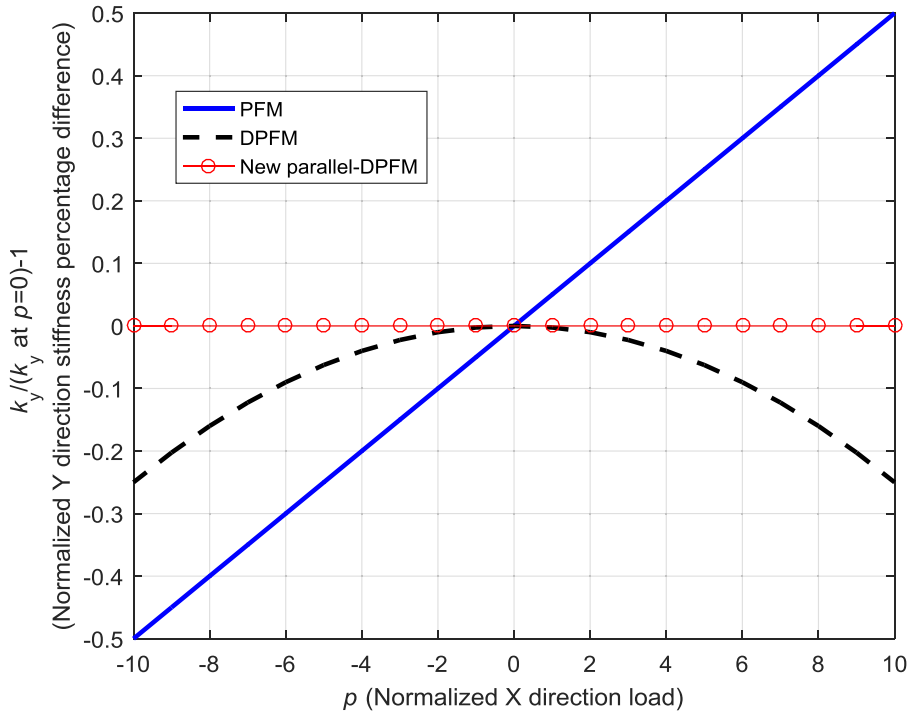


Fig. 3. Load-dependent effect on the motion direction stiffness.

- (b) As can be seen in Eq. (11), the parasitic X direction motion (i.e. error motion) has a kinematic dependence on the rotation about the Z direction and translation along the Y direction. Furthermore, this X direction motion has an elasto-kinematic term dependent on the Y direction displacement and X direction load. Similar to the Y direction, there is no other geometrical parameter apart from t and b involved in the normalized X direction load-displacement relation.
- (c) Shown in Eq. (16), the beam separation parameters w_1 and w_2 for the outer and inner parallelograms both contribute to the rotation, as expected. Increasing these parameters decreases the undesired parasitic rotation. If there is only an X direction force or a Y direction force on the motion stage, there is no parasitic rotation.

3. Design insights and guidelines

In this section, we will first compare the present design with other two traditional designs in a quantitative manner, and then discuss the dimensional parameters related to performance metrics of the mechanism, leading to dimensional optimization.

Of the four dimensionless parameters (t , b , w_1 and w_2) that appear in the normalized X, Y, and Θ_Z direction load-displacement relations, we mainly analyse the influences of t and b since parameters w_1 and w_2 only affect the Z direction rotation.

3.1. Design comparison: Distributed compliance case

In this section, three translational flexure mechanisms with distributed-compliance beams (proposed nested parallel-DPFM, PFM and DPFM) are analysed and compared using the normalised analytical models Eqs. (8), (11), and (A.1)–(A.4). We use $t=1/40$ as an example for this comparison. The comparative results for several performance metrics are shown in Figs. 3–6.

Fig. 3 shows that the X direction force in the new parallel-DPFM (Fig. 2) has no effect on the Y direction stiffness Eq. (8). The DPFM has a smaller load-dependent effect than the PFM. Fig. 4 shows that the PFM has the largest amount of parasitic error motion in the X direction due to the kinematic effect, as opposed to the theoretically zero X direction error motion for both the DPFM and the proposed design. In Fig. 5, we can observe that the DPFM has much larger stiffness degradation in the X direction than that of the proposed design or PFM. The proposed design has the same X direction stiffness degradation as the PFM. Fig. 6 shows the stiffness ratio (k_x/k_y) comparison among the three designs. It is observed that the new/proposed design has the largest k_x/k_y degradation, which is due to the new design's nonlinear increase in stiffness in the motion (Y)

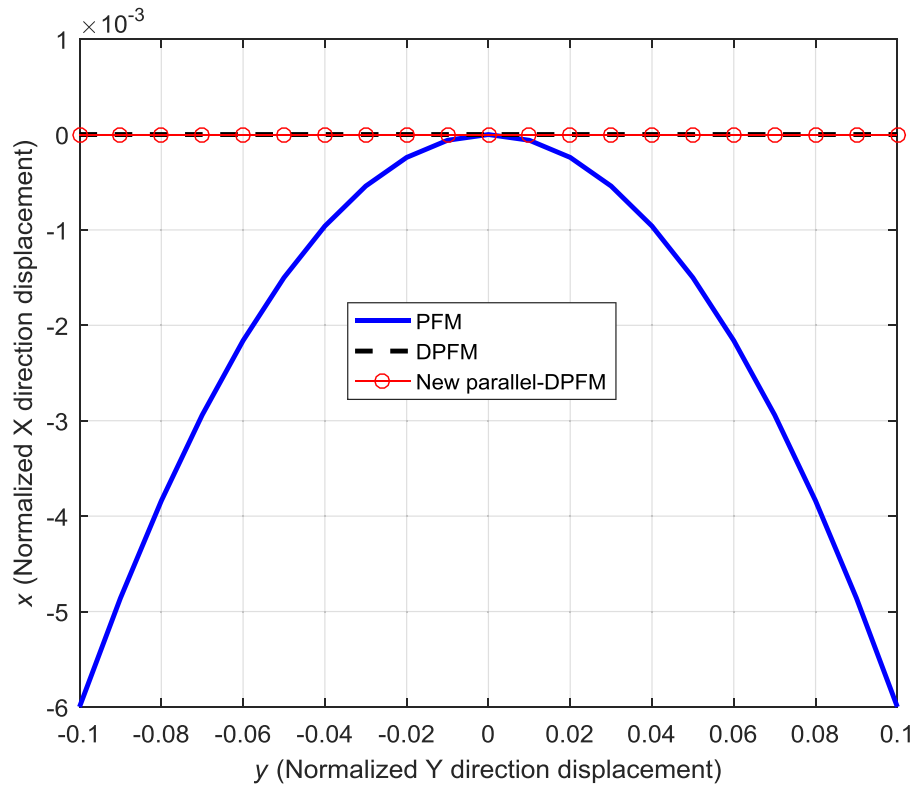


Fig. 4. X direction translation due to kinematic effect (parasitic error motion) for $p=m=0$.

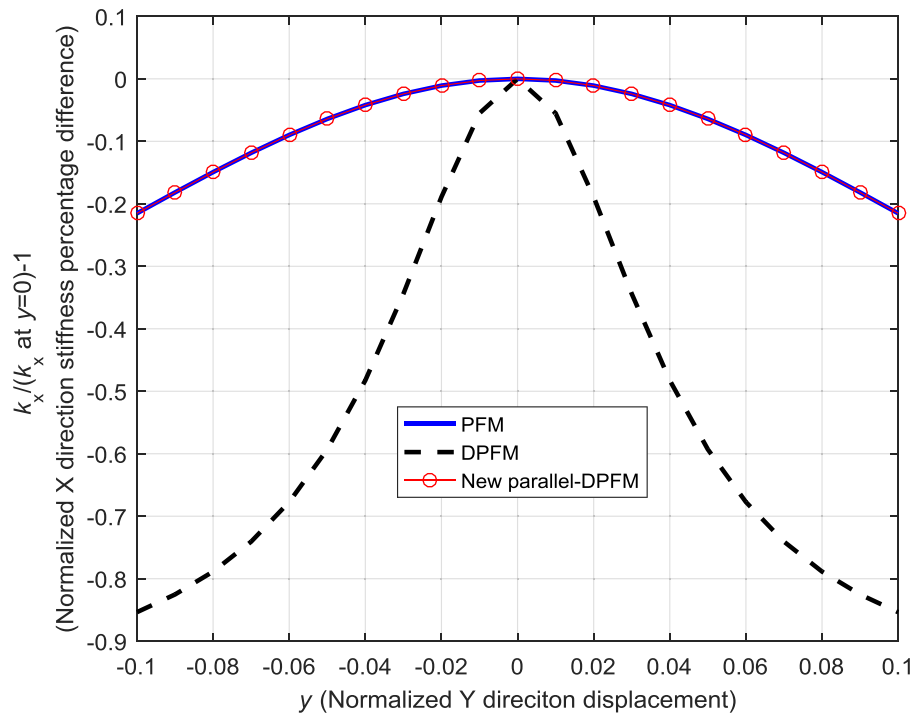


Fig. 5. Stiffness degradation in the X direction.

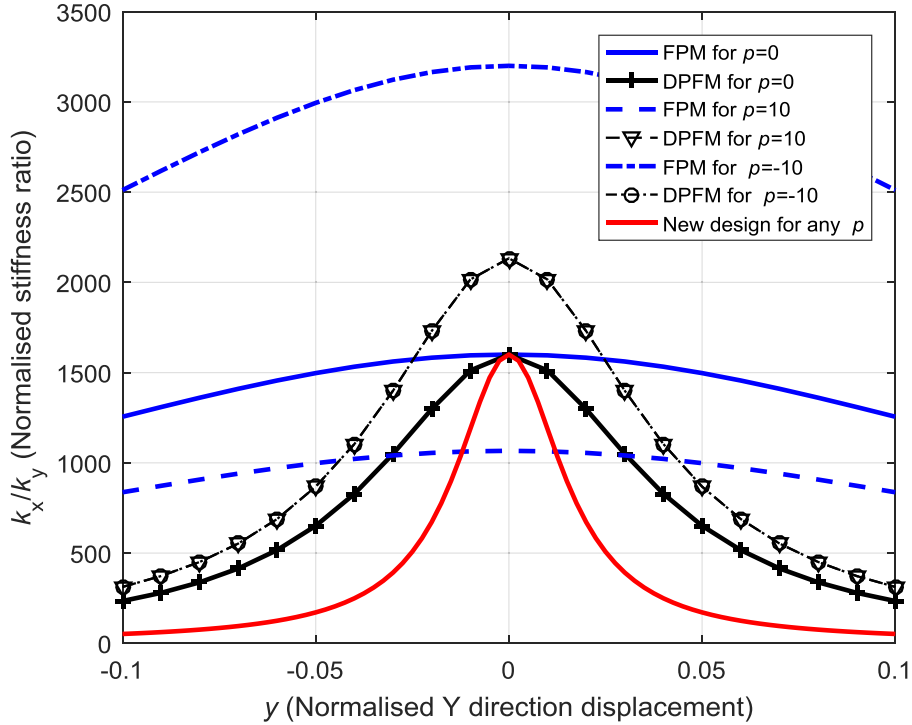


Fig. 6. Stiffness ratio comparison.

direction. Fig. 6 also captures the effect of the X direction force on the stiffness ratio of each design, where the new design has no stiffness ratio change as the X direction force varies.

In order to assess the robustness against buckling for each type of mechanism, Eqs. (8) and (A.2) and (A.4) are re-employed, where an X direction force that causes a zero Y direction stiffness corresponds to the first-order buckling load [5].

For the PFM, using Eq. (A.2), we can derive the buckling load as below:

$$\begin{aligned} 24 + 1.2p &= 0 \\ \Rightarrow p &= -20 \end{aligned} \quad (18)$$

where a minus sign signifies that the compression force leads to buckling.

For the DPFM, using Eq. (A.4), we can derive the buckling load as below:

$$\begin{aligned} (24)^2 - (1.2p)^2 &= 0 \\ \Rightarrow p &= \pm 20 \end{aligned} \quad (19)$$

where the positive and minus signs mean that both the tensile and compression forces lead to buckling.

For the new design, the motion direction stiffness is independent of the bearing direction force as shown in Eq. (8) and Fig. 3. Therefore, in comparison to the results in Eqs. (18) and (19), the new design has the best robustness against buckling. The DPFM is the most vulnerable to buckling since a critical bearing direction force along any of two opposite X directions can lead to buckling.

Fig. 7a shows a compact parallel kinematic XY flexure mechanism based on a 4-PP kinematic topology (P: prismatic joint) [5,7], which is obtained by replacing each kinematic P joint with the proposed new/nested parallel-DPFM (Fig. 2) as the building block. Fig. 7b shows a non-compact parallel kinematic XY flexure mechanism [22] based on the same 4-PP kinematic topology, which is obtained by replacing each kinematic P joint with the traditional parallel-DPFM (Fig. 1c) as the building block. Comparing Figs. 7(a) and (b), we can prove that nested parallel-DPFM design is a better (more compact) building block than the traditional parallel-DPFM from a layout/footprint perspective of more complex XY flexure mechanisms. Given the good performance characteristics of the nested parallel-DPFM building block, buckling is greatly suppressed in this compact XY mechanism, the cross-axis coupling and lost motion of the compact XY mechanism are minimized, and the motion direction stiffness in one axis should be independent of that in another axis. The key limitation of this compact XY design may be the small range of motion due to over-constraint.

Table 1 lists a qualitative summary of the performance characteristics of the PFM, DPFM, traditional parallel-DPFM, and nested parallel-DPFM (new design). This shows that the proposed design fares better in certain performance characteristics

Table 1
Summary of the performance characteristics of several simple distributed-compliance designs.

Characteristic\ Design	Compact Layout (Fig. 7)	Load-dependence (Fig. 3)	Robustness against buckling	Motion (Y) direction Range	X direction error motion (kinematic) (Fig. 4)	X direction stiffness degradation (Fig. 5)	Motion (Y) direction stiffness	Stiffness ratio k_x/k_y degradation (Fig. 6)
PFM	Yes	Strongly Dependent	Unidirectional buckling	Intermediate	Large	Small	Linear	Small
(Serial) DPFM	Yes	Slightly dependent	Bidirectional buckling	Large	Zero	Large	Linear	Large
Traditional parallel-DPFM	No	Independent	No buckling	Relatively small	Zero	Small	Nonlinear	Larger
New design (Nested parallel-DPFM)	Yes	Independent	No buckling	Relatively small	Zero	Small	Nonlinear	Larger

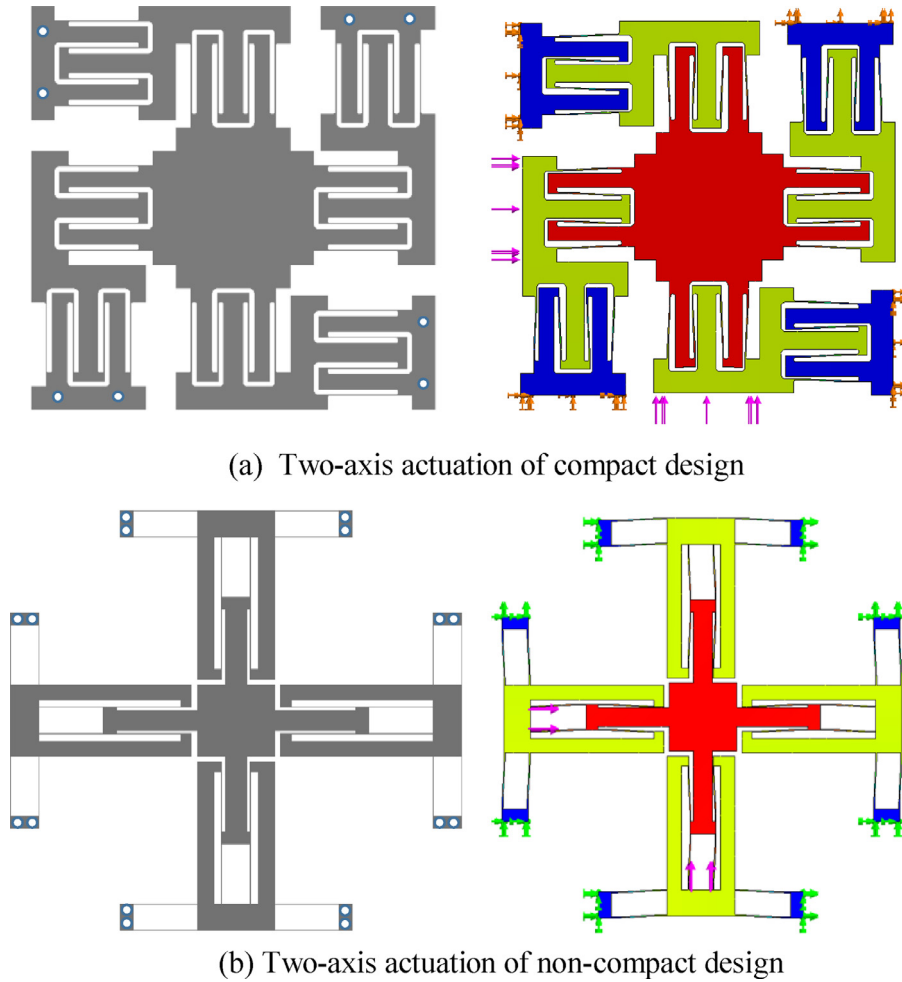


Fig. 7. Comparison between compact XY CPM and non-compact XY CPM.

and worse in others; it can be particularly useful in applications that require a small motion direction stroke but have a critical need for motion direction stiffness that is independent of bearing direction load.

3.2. Beam shape variation

In this section, we use the above analytical models that were derived for any general beam shape to evaluate performance characteristics as a function of the beam shape, specifically the dimensional parameter b in Fig. 2a. Note that the Euler beam model for slender beams is assumed [5,6] in this section to consider the influence of the parameter b . The performance characteristics of interest here include motion (Y) direction load-displacement relation, and ratio of bearing (X) direction stiffness to motion (Y) direction stiffness, which are shown in Figs. 8 and 9, respectively.

Fig. 8 shows the nonlinear stiffening effect in the motion direction with increasing Y direction displacement. We can observe that as the value of b increases from 0 to 0.5, the curve becomes less nonlinear. The value of t also influences the nonlinearity. In order to have a small and relatively constant (actual) stiffness in the motion direction, b should be large, while t should be small. We should point out that the new design has a nonlinear stiffness in the motion direction, which may be more desired for some specified application such as vibration suppression [23] and energy harvesting [24]. However, if the normalised range of motion in the Y direction is limited to $Y/L=y$ (e.g. 0.02 in Fig. 8), the stiffness in the motion direction is almost constant, which is good enough for certain applications that have a critical requirement for insensitivity of motion direction stiffness to bearing direction load.

It is shown in Fig. 9 that the ratio of X direction stiffness to Y direction stiffness drops with increase in the motion direction displacement. The larger the values of b and t , the less significant is the drop in this ratio. Therefore, in order to have a small stiffness ratio drop, b and t should both be large. For a large stiffness ratio in the nominal condition ($y=0$), b and t should both be small. Based on Eq. (17d), Θ_z direction stiffness is $(w_1^2 + w_2^2)/2$ times X direction stiffness. Therefore,

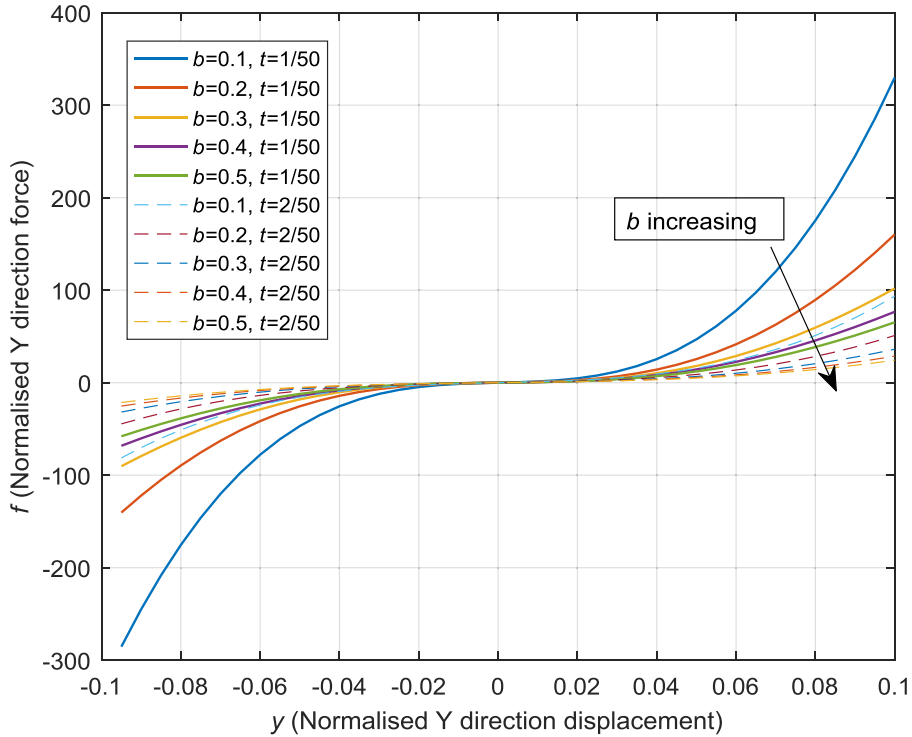


Fig. 8. Y direction force against Y direction displacement.

the ratio of Θ_Z direction stiffness to Y direction stiffness also follows a trend similar to that in Fig. 9, and is not separately plotted in this paper.

In addition, we investigate two terms that affect the motion in the bearing directions (X and Θ_Z) but do not appear in the stiffness equations Eq. (17d). The coefficient $(k_{11}^{(1)}/2 + k_{12}^{(1)})$ for the Z direction rotation Eq. (16) couples the X direction force and the Y direction displacement to influence the Θ_Z direction displacement even in the absence of a moment m . When expressed in terms of b , it is seen that this coefficient: $\frac{45-180b+300b^2-240b^3+80b^4}{10(3-6b+4b^2)^2}$ is constant and equal to half for all values

of b , despite the individual $k_{11}^{(1)}$ and $k_{12}^{(1)}$ coefficients varying with b significantly as shown in Appendix B. Fig. 10 captures the contribution of the second term, which is a kinematic term, in the X direction translation Eq. (11). Here we plot the coefficient of θ which is a function of b , t , and motion direction displacement y . This coefficient $(k_{11}^{(1)}y/2(1 - k_{11}^{(2)}k_{33}y^2))$ increases with y , and is always equal to zero when $y=0$. A larger value of t generally leads to a more linear curve. For a larger value of t , b has a smaller influence on the plotted coefficient. However, for a smaller value of t , b has a noticeable effect on the coefficient. Given that Θ_Z direction is the DoC direction, θ is typically at least 10^{-2} times less than the motion direction displacement y Eq. (16), the second (i.e. kinematic) term in Eq. (11) is approximately of the order of 5×10^{-5} and is the only remaining term in Eq. (11) in the absence of an X direction force. The small value of this kinematic term shows the significant reduction in the X direction parasitic error motion in the new design compared to a PFM.

Next, a set of dimensions for the new mechanism can be chosen for the FEA validation and prototype testing validation in the subsequent sections.

- In light of the above findings and trade-offs for desired *stiffness characteristics* (i.e., a small and relatively constant stiffness in the Y direction stiffness, and a small drop of ratio of X direction stiffness to Y direction stiffness and a large stiffness ratio in the nominal condition), we select $b = 1/2$ to achieve a distributed-compliance design and decide to use the smallest possible value of t that is allowed by machining capabilities.
- Selecting $b = 1/2$, as justified above, is also favourable from a *large range of motion* point of view. Based on the stress criterion below, that takes into account the stress resulting from the overconstraint in the mechanism [10],

$$\sigma_{\max} = \left| \left(6 + \frac{0.06y^2}{1/d + y^2/700} \right) yEt/2 \right| + \left| \left(\frac{0.6y^2}{1/d + y^2/700} \right) Et^2/12 \right| < \sigma_s \quad (20)$$

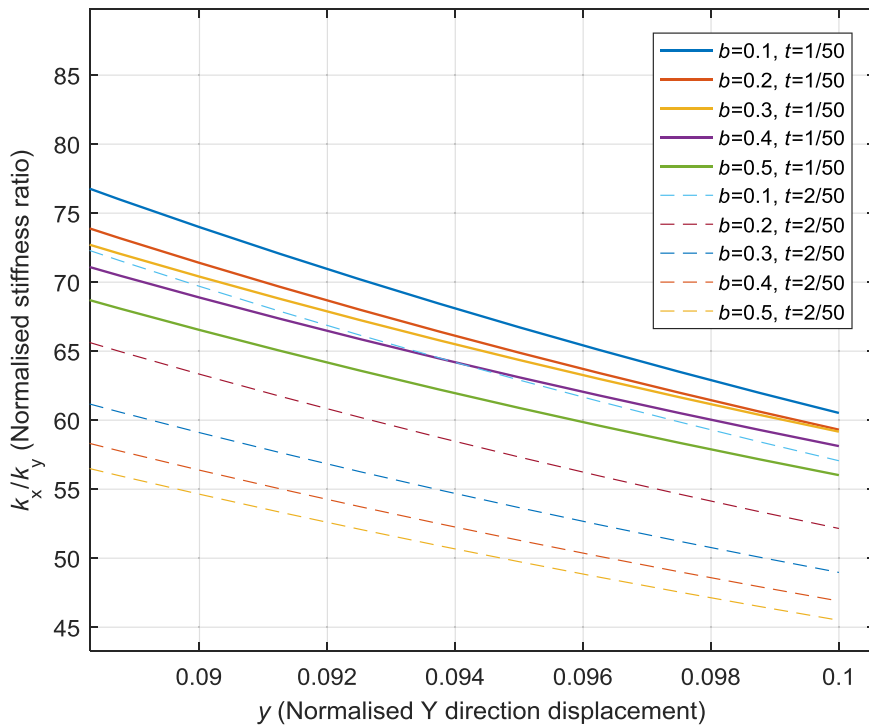
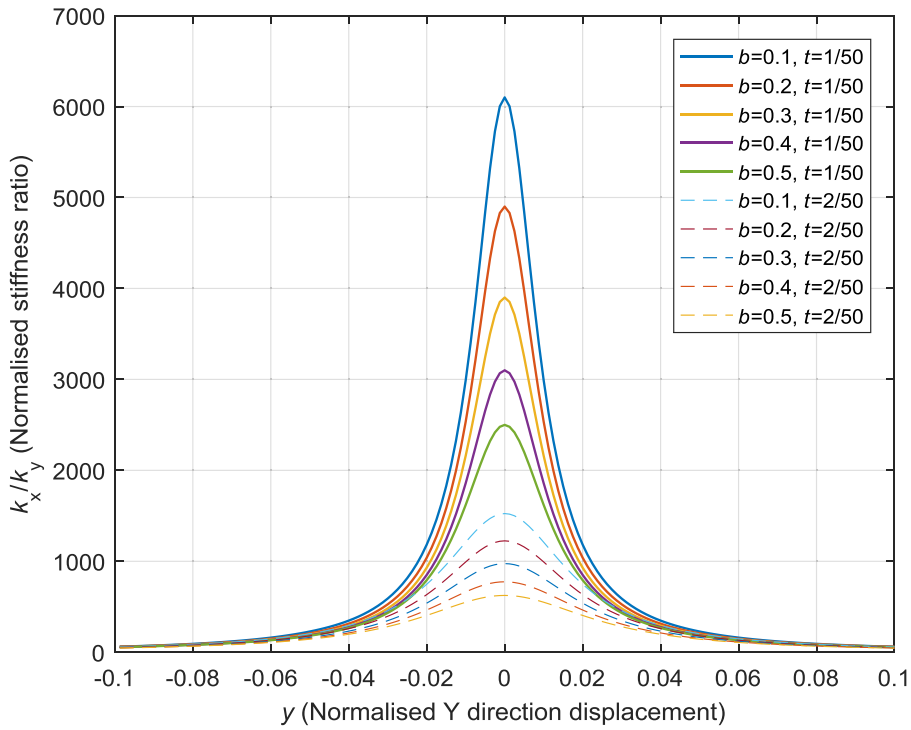


Fig. 9. Ratio of X direction stiffness to Y direction stiffness.

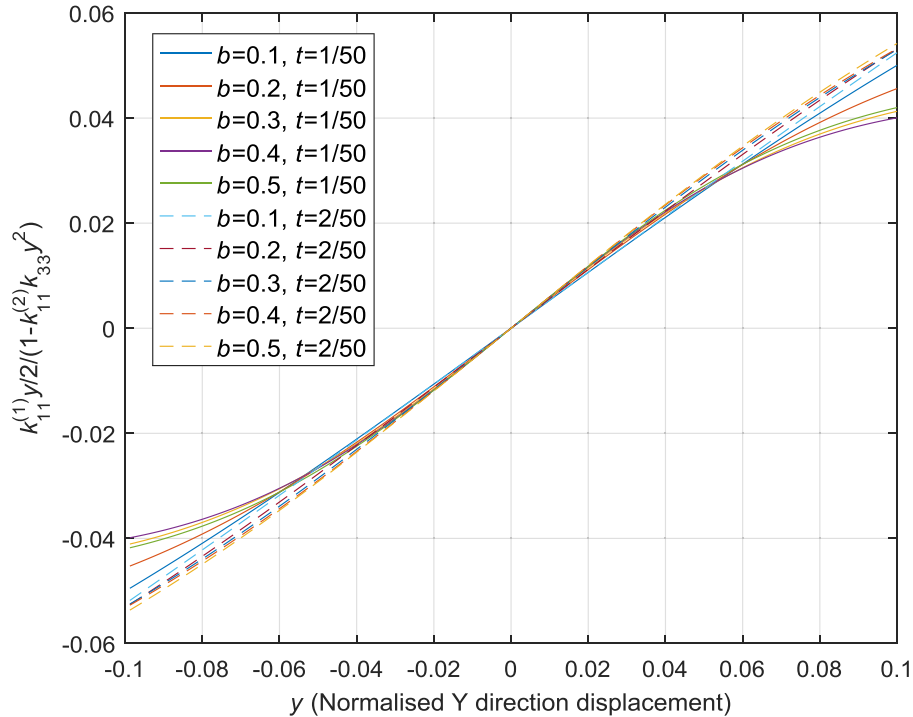


Fig. 10. Term related to X direction motion.

where σ_s is the yield strength, $d = 12/t^2$, and y is the range of motion. We can conclude that both the ratio of actual beam length to the actual beam thickness (L/T) and the ratio of yield strength to Young's modulus (σ_s/E) for the material of compliant members should be large.

Given the two criteria (stiffness and range of motion), the FEA study and prototype testing are conducted with the following geometrical parameters:

$b = 1/2$ (distributed-compliance);

$T = 0.75$ mm (the smallest thickness to be discussed in Section 5);

$W_1 = 54.25/2$ mm, $W_2 = 19.75/2$ mm, $L = 45$ mm (to achieve compact desktop-size design and millimetre range of motion as shown in Section 4); and

$U = 10$ mm (a standard depth of the material plate).

4. Finite element analysis validation

The commercial software, COMSOL 5.0, was used for the purpose of FEA. In COMSOL, we created the above-described mechanism design without any fillets, which conforms with the closed-form modelling assumption of beam geometry in Section 2. Although adding small fillets can reduce stress concentration and is inevitable in any manufacturing process, it has a negligible influence on the modelling of distributed-compliance beams. We used Young's modulus, E , of 70 GPa, Poisson's ratio of 0.33, and yield strength of 260 MPa (corresponding to US standard AL6061) for the material of compliant members. The material of the rigid segments was chosen to be 10,000 times stiffer than that of the compliant members (Fig. 2) to allow a check on the analytical model. We selected the nonlinear option in FEA, and employed the 10-node tetrahedral element and automatic fine meshing (i.e., maximum element size 7.44 mm (employed in the rigid segment of the beam), minimum element size 0.93 mm (employed in the compliant segments of the beam), maximum element growth rate 1.45, curvature factor 0.5, and resolution of narrow regions 0.6).

The FEA simulation results using COMSOL are shown in Fig. 11 and discussed as follows:

- Fig. 11a shows that the Y direction analytical model (Eq. (8)) matches the FEA model very well, and that the impact of the X direction load on Y direction displacement and stiffness is indeed unnoticeable/negligible.
- Fig. 11b captures the X direction displacement comparison between the analytical model (Eq. (11)) and the FEA simulation under the condition of no pure moment applied. Two models have an acceptable agreement. The FEA model for a smaller X direction force follows the corresponding analytical model better. The FEA simulation shows a slightly smaller nonlinear elasto-kinematic effect than that of the analytical model.

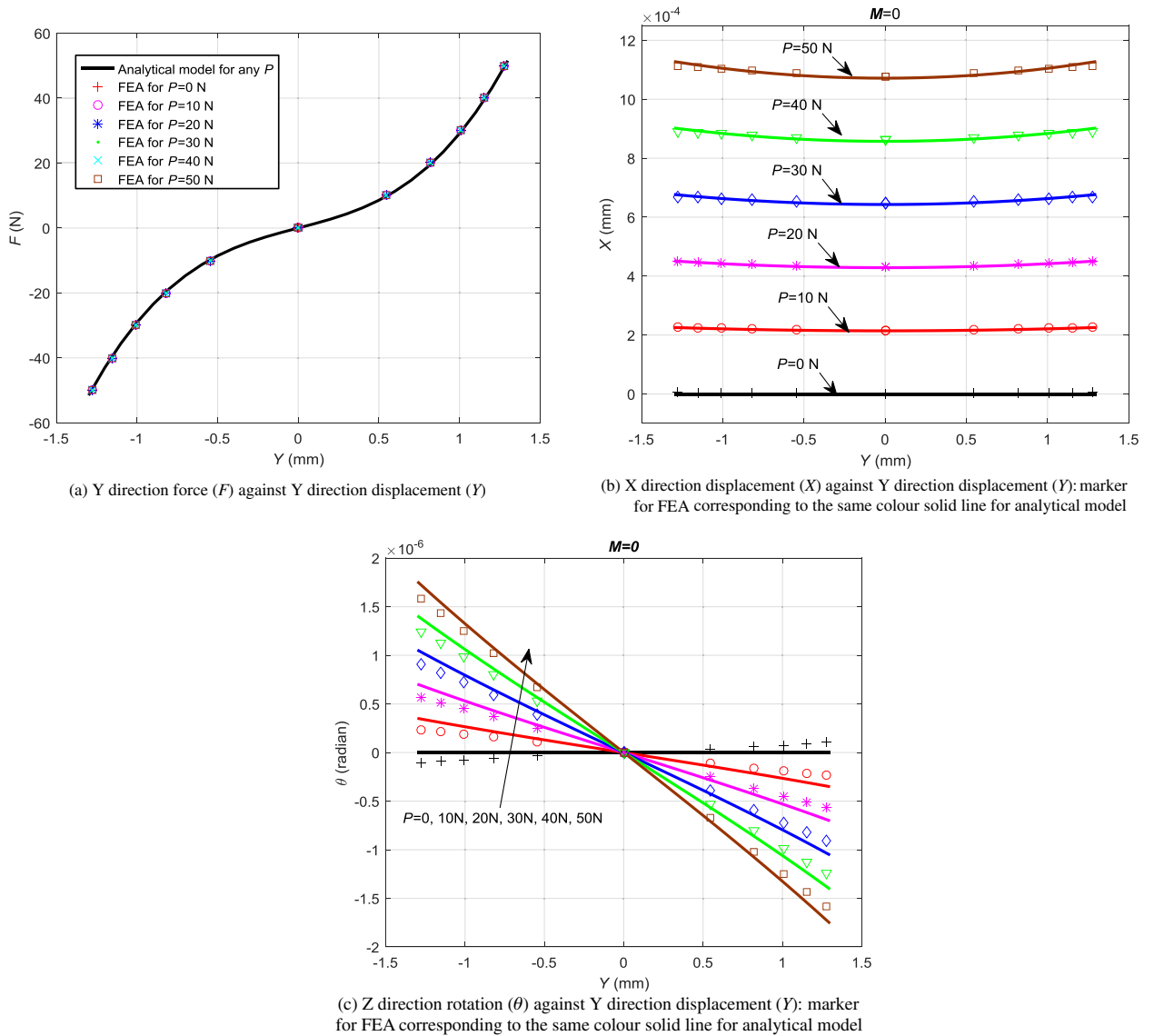


Fig. 11. Comparison with FEA.

(c) The Θ_z direction results are compared in Fig. 11c under the condition of no pure moment applied. The FEA simulation follows the trend of the analytical model, and is slightly smaller than the analytical model in magnitude (except when there is no X direction force). In the presence of an X direction force, the FEA model tends to be more linear than the analytical one.

On possibility for the discrepancy between the two models shown in Fig. 11b and c is that the BCM truncates the axial load terms to the first order assuming a limit on the axial load ($|p| \approx 10$) [5,6]. However, in this design because of over-constraint the internal axial load can be higher than this limit so that the first order truncation used in the BCM may lead to some discrepancy. Another possibility is due to the simplification in the manual derivations in Section 2.

The range of Y direction motion is determined based on the stress criterion (Eq. (20)) where the maximum stress should be less than the yield strength (260 MPa in this study). As seen in Fig. 12, the maximum allowable range of motion is about $[-1.7 \text{ mm}, 1.7 \text{ mm}]$ (i.e., ± 0.038 normalised displacement) without considering stress concentration. Considering a conservative design to avoid material yield failure and an actuation effort limit in the motion direction (50 N is the force sensor limit in our experiment), we selected $\pm 1.25 \text{ mm}$ (i.e., ± 0.028 normalised displacement) as the maximum actual Y direction displacement for the COMSOL FEA simulations, as well as subsequent experimental testing. The experimental testing in Section 5 confirms that a 1.25 mm range of motion is feasible without causing yield failure.

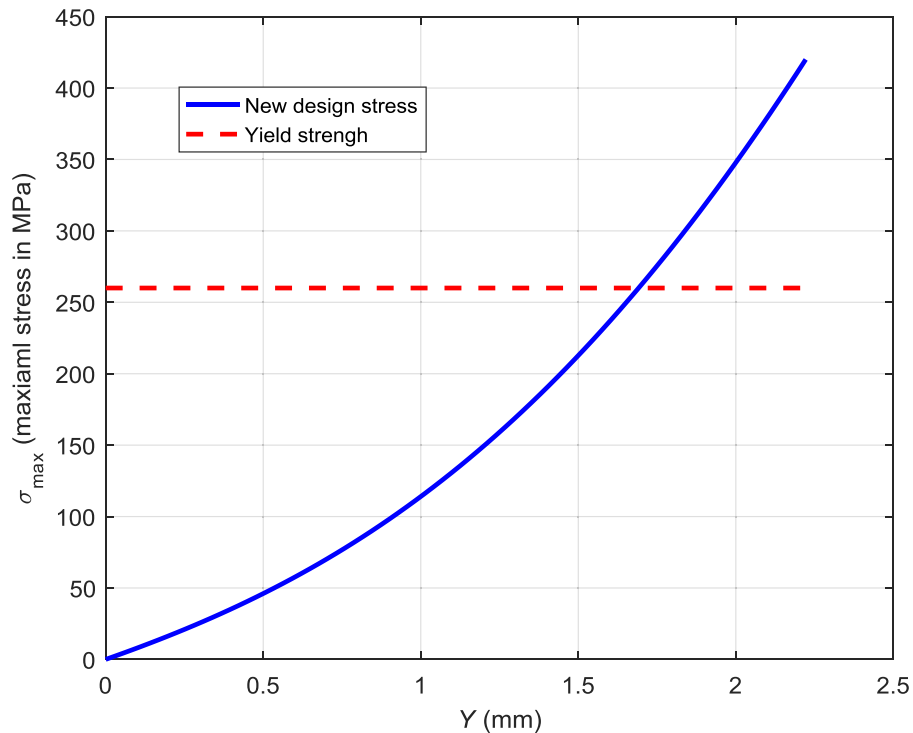


Fig. 12. Stress analysis when no bearing direction force.

5. Design, fabrication, and assembly of experimental hardware setup

5.1. Fabrication of the nested parallel-DPFM prototype

A 4-axis CNC milling machining is used to fabricate the monolithic nested parallel-DPFM proposed in this paper. This does not require a significant amount of set-up work and is less expensive than wire electric discharging machining (EDM). However, while fabricating beam thicknesses of less than 0.5 mm is standard with wire-EDM, similar dimensions are challenging to achieve with CNC milling, due to contact-based metal cutting. 0.75 mm was the smallest thickness that we could satisfactorily fabricate using the CNC mill. Furthermore, with the CNC mill, a fillet radius is introduced at the corners due to the diameter of the cutter. In this work, a 2 mm diameter cutter was used that resulted in fillet radii of 1.0 mm. These small fillets are the deviation from the closed-form modelling and FEA, but do help relieve stress concentration. A detailed discussion on CNC milling for the fabrication of compliant mechanisms is presented in [Appendix C](#).

5.2. Selection of material and dimensions

The dimensional parameters used in the FEA study and in the fabricated prototype are listed at the end of [Section 3](#). Aluminium alloy AL6082-T651 (EU standard, equivalent to the US standard AL6061-T651) from Aalco was chosen for the prototype material, with a relatively large ratio of yield strength to Young's modulus (0.0037). This material is a good choice for flexure mechanisms used in precision instruments due to the material's economic cost, good strength, low internal stresses and phase stability [5].

5.3. Selection of sensors, actuation and data acquisition

We set up a static testing system for sensing forces and displacements, applying loads, and acquiring data of the nested parallel-DPFM prototype. This system is effective and economic and can test the force-displacement relations in the motion (Y) direction with considering the load-dependent effect from the bearing (X) direction force. The actuation displacement (Y) in the motion (Y) direction of the flexure prototype is loaded by a micrometer (Moore & Wright). This manual micrometer has a 2 μm displacement resolution and a more than 10 mm actuation range. We employed a force sensor (Vernier dual-range) to detect the motion direction force applied on the motion stage. This force sensor has a 0.05 N resolution and a 50 N measuring range, which connects to a sensor interface (LABQUEST 2) to acquire data. Another displacement sen-

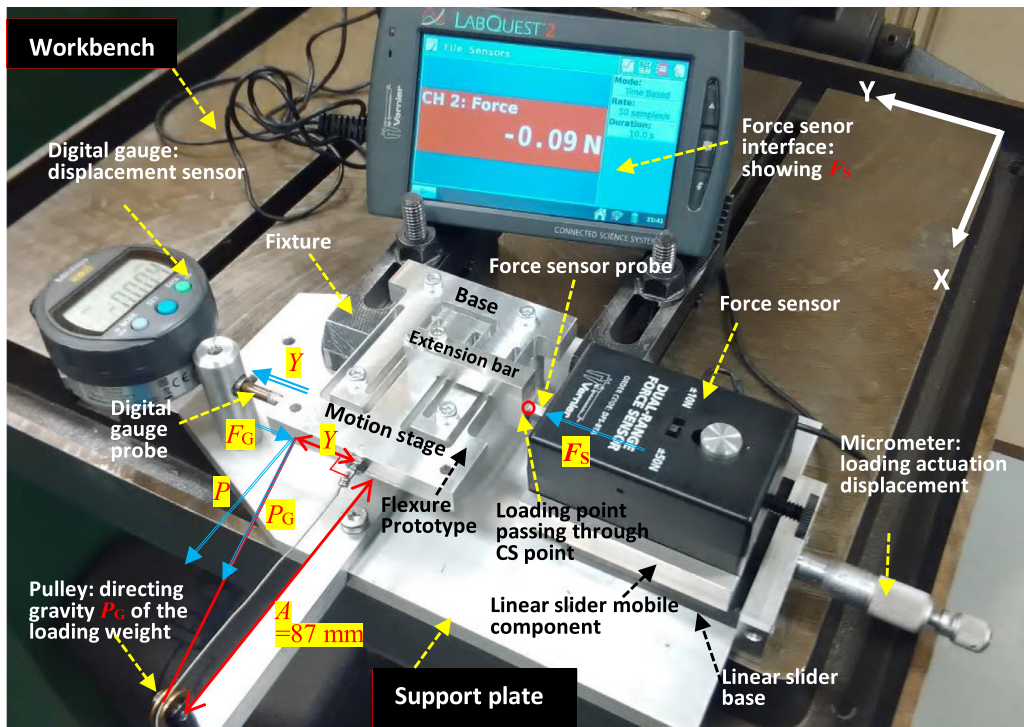


Fig. 13. Prototype and experimental testing setup of a new distributed-compliance parallel-DPFM.

sensor, a digital gauge (Mitutoyo Absolute) with a resolution of $1 \mu\text{m}$ and negligible spring force of $0.04\text{--}0.07 \text{ N}$, is used to measure the output displacement in the motion direction. The force in the bearing (X) direction is applied by a loading weight.

5.4. Assembly of hardware

The fabricated parallel-DPFM prototype is first fixed to a large support plate by bolting. The support plate is then connected to a horizontal workbench by a fixture. The base of a linear slider (including base and mobile component) sits on the support plate. The mobile component of the linear slider is actuated by the micrometer. The force sensor stacks on top of the slider's mobile component. We ensure that the probe of the force sensor contacts with the motion stage extension bar of the parallel-DPFM, and that the loading force can go through the CS point (defined in Fig. 2). The dial gauge is arranged in a way that its probe touches another side of the motion stage of the parallel-DPFM, in order to directly test the motion direction displacement. The loading weight in the vertical direction is directed by a pulley (supported by a fixed arm) to provide a horizontal bearing (X) direction force. The prototype and experimental testing setup are shown in Fig. 13.

6. Experimental validation

Due to the limitation of resolution of the available sensors in our lab, it was not possible to measure the tiny X direction displacements accurately. Since the Y direction forces and displacements are much larger in magnitude, these were experimentally measured and therefore only the motion direction (Y) stiffness will be discussed in experiment.

6.1. Initial setup

The dial gauge probe is designed to touch the flexure mechanism before conducting each experimental testing. Based on the home position of the flexure mechanism (no deformation) the dial gauge (displacement sensor) and the force sensor interface are both reset to zero initially, while the force sensor probe is detached from the extension bar. Then by turning the micrometer screw and monitoring the force sensor interface simultaneously, we can make the force sensor probe just touch the extension bar where the reading of the force sensor is about one or two resolution(s) of the force sensor.

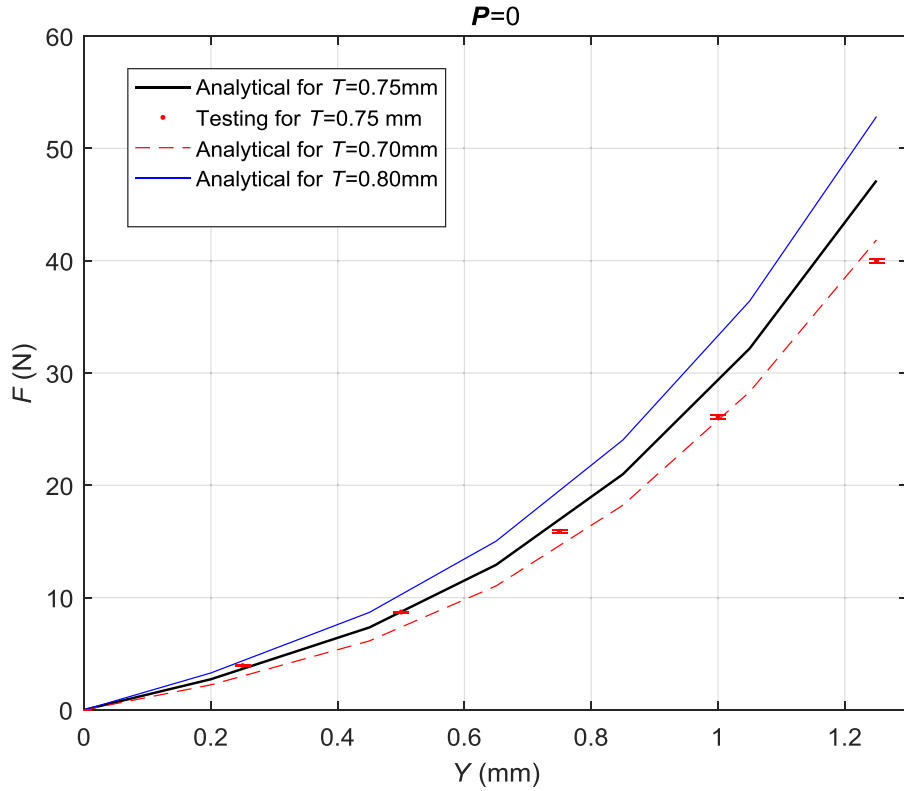


Fig. 14. Comparisons when no bearing direction force.

6.2. Experimental procedure

6.2.1. Measurement without bearing direction force

We turn the micrometer screw while observing the dial gauge reading (starting from zero). The motion direction displacement reading is set up at an equal incremental step of 0.25 mm, and the corresponding force sensor measurement is recorded at each step. We stop turning the micrometer when the maximum displacement of 1.25 mm in the motion direction is reached. We repeated the same procedure above three times with the average force data presented in the graph (Fig. 14).

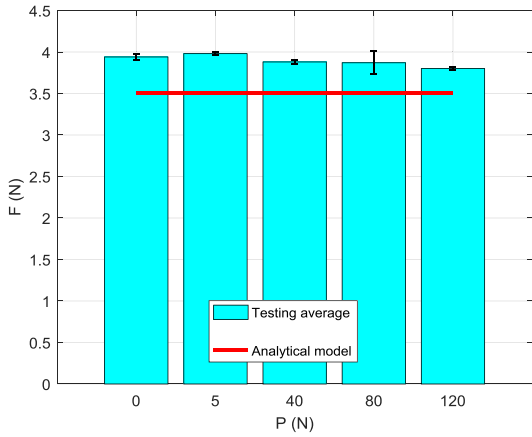
6.2.2. Measurement with bearing direction force

We follow the same procedure as the above scheme for the new testing scheme, except adding a loading weight to exert a bearing (X) direction force. At each incremental step of 0.25 mm in the motion (Y) direction that is maintained constant, we increase the bearing direction forces from 5 N, 40 N, 80 N up to 120 N, while recording the corresponding forces in the motion direction. Under this testing scheme, the forces in both Y and X directions cannot be directly obtained, but are calculated as detailed below.

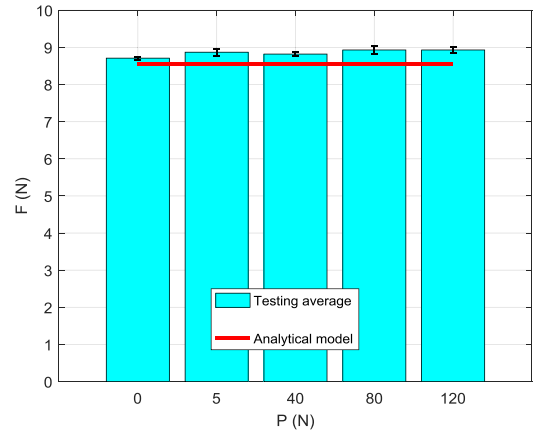
The actual bearing (X) direction force (P) exerted on the prototype is provided by the loading weight (P_G). Due to the motion direction displacement (Y), the gravity force of the hung weight, P_G , also results in a component force (F_G) that contributes to the (resultant) reading of the Y direction force sensor interface ($F_S = F + F_G$ is the sensor reading). The force sensor shows the reaction force of the resultant motion direction force. Therefore, the actual force in the motion (Y) direction that contributes to the motion direction displacement (Y) is $F = F_S - F_G$. Note that Y , in an italic form, is used here to represent an actual displacement as opposed to the upright form Y representing direction. F and P can be calculated as below so that the load-dependent effect can be plotted in Fig. 15.

$$\begin{cases} F = F_S - F_G = F_S - \frac{Y}{\sqrt{Y^2+A^2}}P_G \\ P = \frac{A}{\sqrt{Y^2+A^2}}P_G \end{cases} \tag{21}$$

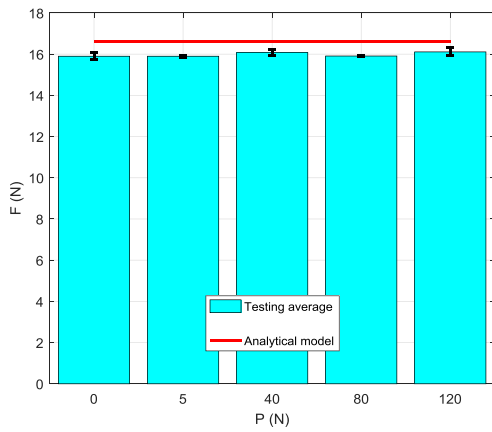
where A , the supporting arm length, and other symbols are indicated in Fig. 13.



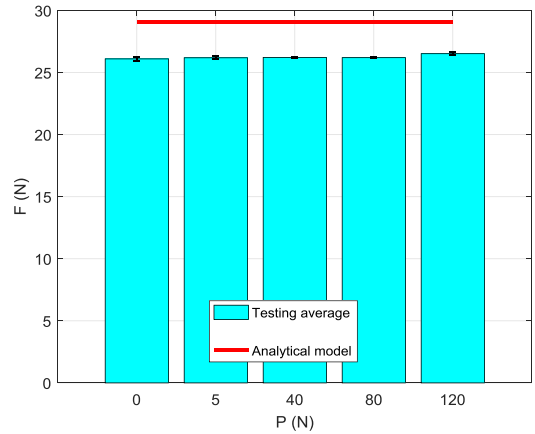
(a) $Y=0.25$ mm



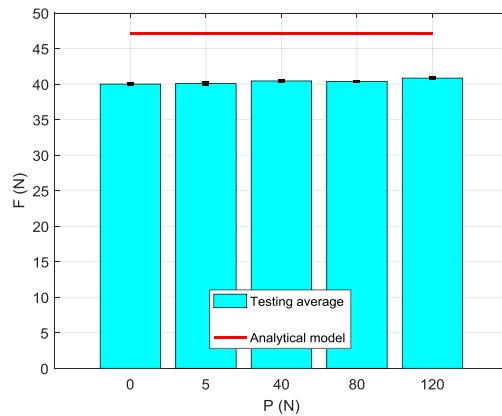
(b) $Y=0.50$ mm



(c) $Y=0.75$ mm



(d) $Y=1.0$ mm



(e) $Y=1.25$ mm

Fig. 15. Load-dependent effect testing.

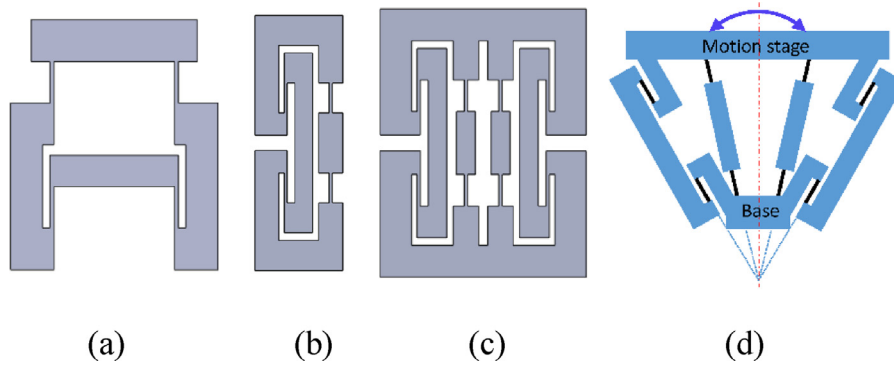


Fig. 16. Other flexure mechanisms.

6.3. Experimental measurement results

Fig. 14 shows the comparison between the analytical model and the measurement result, where the discrepancy rises with the increase of the motion (Y) direction displacement. It can be seen that the 1.25 mm range of motion ($0.028L$) in the physical testing is feasible for the overconstrained design, and that the nonlinear phenomenon is still significant over this range of motion that supports the necessity of nonlinear modelling. During a small range of displacement (< 0.5 mm), the analytical model matches the measurement result satisfactorily. This discrepancy suggests that the analytical model has a stronger nonlinearity than the measurement result, i.e., the analytical model captures greater stiffness compared to the measurement results. The analytical results for another two cases, $T=0.70$ mm and $T=0.80$ mm, are also presented in Fig. 13. We can observe that the measurement result (i.e., a nominal fabrication thickness of $T=0.75$ mm) is closer to the analytical model when $T=0.70$ mm. This may suggest that there is a certain fabrication error in beam thickness that makes the actual beam slightly thinner and therefore more compliant. Conversely, the added fillets (due to milling machining) make the fabricated beam a little shorter and therefore stiffer than the one modelled. However, the softening effect due to the reduced beam thickness is stronger than the stiffening effect due to the added fillets; therefore the resulting fabricated beams render overall greater compliance. Note that the assumed rigid segments in the fabricated prototype also produce tiny deformation in reality and therefore non-zero compliance, which can also contribute to the discrepancy between the analytical model and the measurement result.

In order to illustrate the elimination of load-dependent effects in the nested parallel-DPFM, Fig. 15 shows the tested motion (Y) direction force (F) against the bearing (X) direction force (P) at different motion direction displacements (Y). As observed, the bearing direction force has very little influence on the motion direction force, which validates the elimination of load-dependent effects.

7. Conclusions

This paper reports a compact parallel-DPFM with a general beam shape. It is designed by using a nested arrangement of two parallelogram modules in parallel. The new design eliminates dependence of motion direction stiffness on bearing direction load, provides robustness against the buckling, and suppresses the bearing direction parasitic error motion. Analytical (closed-form) models have been derived to analyse several performance metrics and enable design insights. A hardware setup has been designed to experimentally validate the closed-form model. Nonlinear FEA and/or physical measurement results confirm the modelling accuracy as well as the elimination of load-dependent effect on motion direction stiffness. The proposed design is valuable in applications where insensitivity of motion direction stiffness to bearing direction load is critical. However, the new design presents shortcomings in that the motion direction stiffness is nonlinear and the range of motion is limited due to over-constraint.

We can further copy similar ideas to design general beam flexure mechanisms, as shown in Fig. 16 as shown in [25], which is the topic of future work. Fig. 16a, b and c show three single-axis translational mechanisms and Fig. 16d shows a single-axis rotational mechanism. As can be seen, half of compliant members are always in compression and half in tension, regardless of the direction of the bearing direction force applied on the mechanism. Therefore, the load-dependent effect can be alleviated.

Acknowledgements

Mr. Tim Power and Mr. Michael O'Shea in School of Engineering at University College Cork (UCC) are greatly appreciated for their contribution to fabricating the flexure mechanism and assembling the experimental test rig. In particular, Tim contributes to writing [Appendix C](#). Dr. Richard Kavanagh in UCC is acknowledged for his help in refining the English of this paper. The authors also thank Dr. Haiyang Li for his assistance in running COMSOL.

Supplementary materials

Supplementary material associated with this article can be found, in the online version, at doi:[10.1016/j.mechmachtheory.2019.103593](https://doi.org/10.1016/j.mechmachtheory.2019.103593).

Appendix A. Other closed-form equations

References [5–7] have derived the closed-form analytical equations of both the PFM and the DPFM with distributed compliance, as summarized below.

The PFM's solutions for the two translational displacements, based on the coordinate system in [Fig. 1a](#), are as follows

$$x = \frac{p}{2d} - 0.6y^2 + \frac{py^2}{1400} \quad (\text{A.1})$$

where on the right-hand side, the first, second and third terms represent the pure elastic effect, the pure kinematic effect (parasitic error motion) due to the motion direction displacement, and the elasto-kinematic effect, respectively.

$$y = \frac{f}{24 + 1.2p} \quad (\text{A.2})$$

where the denominator on the right-hand side shows the load-dependent stiffness effect. Therefore, the X direction force can have a load-dependent effect on the Y direction displacement

The DPFM's solutions for the two translational displacements, based on the coordinate system in [Fig. 1b](#), are as follows

$$x = \frac{p}{d} + \frac{85py^2}{2800} \quad (\text{A.3})$$

where the kinematic effect term vanishes in the right-hand side of the equation.

$$y = \frac{48f}{(24)^2 - (1.2p)^2} \quad (\text{A.4})$$

where the load-dependent effect remains in a reduced form when observing the denominator of the right-hand side of the equation.

Appendix B. Beam characteristic coefficients [6]

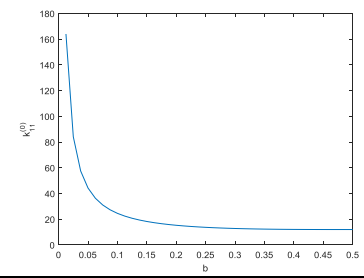
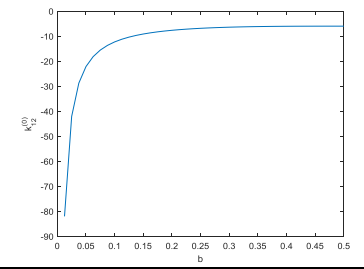
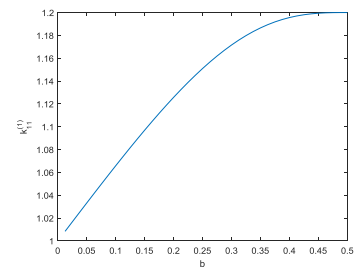
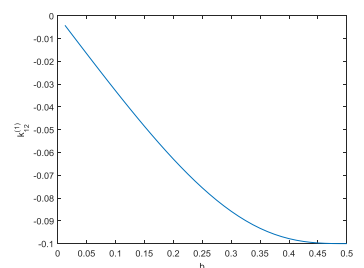
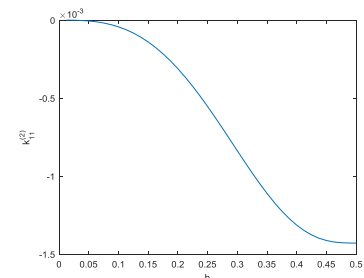
Coefficient	Function	Case of $b=0.5$	Function curve
$k_{11}^{(0)}$	$\frac{6}{b(3-6b+4b^2)}$	12	
$k_{12}^{(0)}$	$-\frac{3}{b(3-6b+4b^2)}$	-6	
$k_{11}^{(1)}$	$\frac{3(15-50b+60b^2-24b^3)}{5(3-6b+4b^2)^2}$	1.2	
$k_{12}^{(1)}$	$-\frac{b(15-60b+84b^2-40b^3)}{5(3-6b+4b^2)^2}$	-0.1	
$k_{11}^{(2)}$	$-\frac{2b^3(105-630b+1440b^2-1480b^3+576b^4)}{175(3-6b+4b^2)^3}$	-1/700	
k_{33}	$\frac{6}{bt^2}$	$12/t^2$	No need to plot the simple function here

Fig. B.1. Beam characteristic coefficients.

Appendix C. Thin wall machining in compliant mechanisms using CNC milling machining

Milling of thin walls requires special attention. This is especially relevant when the materials are of a ductile material because the deflection of the part from the tool can seriously hamper the shearing action necessary for accurate cutting.

In the case of machining compliant mechanisms in our work, we have often machined thin wall structures where the wall thickness has to be as thin as 0.75 mm, and we wish to maintain an accuracy of ± 50 μm along the wall. In most cases, the wall is either on the perimeter of the part or else it is a wall shared by two pockets.

Traditional manufacturing would entail machining one pocket with a roughing cut to full depth then carrying out a finishing/second pass, leaving 0.1 mm for the second pass. Then the second pocket would be machined using the same principle. It can easily be visualised that when machining the second finishing pass, the wall will only be supported at either end. Hence it can be classified as a simply supported beam and naturally the bending moment will be at a maximum in the centre. These properties will make it very difficult to machine aluminium to within our required tolerances and it will make working with Polycarbonate to this specification almost impossible.

For this reason, we have adapted our method of manufacture to ensure that the wall is uniformly supported along its entire length at all stages of fabrication. This is carried out by machining the first pocket in the conventional manner, then a core is manufactured and placed into the first pocket to simulate a solid block of material when the second pocket is being machined. In the case of the perimeter, cores are placed in all adjacent pockets then the outside profile is machined. We have found that a block manufactured to between 10 μm and 15 μm under the nominal pocket size results in a sliding fit that allows us to achieve our tolerances. Blocks manufactured to a “line to line fit” resulted in some cases in stress fractures in the mechanism after the blocks were pressed out. These must be avoided lest the stress concentrations result in premature failure but also for the generation of accurate results for which a homogenous structure is crucial.

Furthermore, we also employ a technique sometimes used in turbine blade manufacturing. This is a two-stage finishing technique, which has generated very satisfactory results. It involves machining the pocket to full depth but leaving a 3 mm finishing allowance on the wall. This allowance is then removed in two passes in depths of 1 mm (the smaller depth, the better quality), the first pass at each depth leaving 0.1 mm for the second pass to remove. Hence the wall at that depth is finished before moving to the next 1 mm deep cut. This ensures that the material is supported both from the back by either the solid wall or the insert and underneath by a 3 mm thick wall. A drawback to our use of this technique is that there is no material underneath the final depth cut.

Using the method of inserting a core will ensure we can machine within spec, while coupling this to the “clear Z” (waterline machining) finishing method ensures there is minimum tool deflection and it also allows for easier chip removal. This is important in the fabrication of plastics because the small final finishing chip can easily burn due to friction and increase the surface roughness of the sidewall but is not as relevant in the present metal prototype.

In summary, we have found these methods complement each other, resulting in accurate, high quality parts.

References

- [1] L.L. Howell, *Compliant Mechanisms*, John Wiley & Sons, 2001.
- [2] N. Lobontiu, *Compliant mechanisms: Design of Flexure Hinges*, CRC press, 2002.
- [3] D.B. Hiemstra, G. Parmar, S. Awtar, performance tradeoffs posed by moving magnet actuators in flexure-based nanopositioning, *ASME/IEEE Trans. Mechatron.* 19 (1) (2014) 201–212.
- [4] M. Olfatnia, S. Sood, J. Gorman, S. Awtar, Large stroke comb-drive actuators based on the clamped paired double parallelogram flexure, *IEEE/ASME J. Micro Electro Mech. Syst.* 22 (2) (2013) 483–494.
- [5] S. Awtar, *Synthesis and Analysis of Parallel Kinematic XY Flexure Mechanisms* Sc.D Thesis, Massachusetts Institute of Technology, Cambridge MA, December 2003.
- [6] S. Awtar, A.H. Slocum, E. Sevincer, Characteristics of beam-based flexure modules, *J. Mech. Des.* 129 (6) (2007) 625–639.
- [7] S. Awtar, A.H. Slocum, Constraint-based design of parallel kinematic XY flexure mechanisms, *J. Mech. Des.* 129 (8) (2007) 816–830.
- [8] H. Zhao, S. Bi, Accuracy characteristics of the generalized cross-spring pivot, *Mech. Mach. Theory* 45 (10) (2010) 1434–1448.
- [9] H. Zhao, S. Bi, Stiffness and stress characteristics of the generalized cross-spring pivot, *Mech. Mach. Theory* 45 (3) (2010) 378–391.
- [10] G. Hao, H. Li, Extended static modeling and analysis of compliant compound parallelogram mechanisms considering the initial internal axial force, *J. Mech. Robot* 8 (4) (2016) 041008.
- [11] E.G. Merriam, L.L. Howell, Non-dimensional approach for static balancing of rotational flexures, *Mech. Mach. Theory* 84 (2015) 90–98.
- [12] E.G. Merriam, J.M. Lund, L.L. Howell, Compound joints: behavior and benefits of flexure arrays, *Precis. Eng.* 45 (2016) 79–89.
- [13] Y.K. Yong, S.R. Moheimani, B.J. Kenton, K.K. Leang, Invited review article: high-speed flexure-guided nanopositioning: mechanical design and control issues, *Rev. Sci. Instrum.* 83 (12) (2012) 121101.
- [14] G. Hao, A multiaxis, large-output, sensing framework of integrating linear optical encoders for nanopositioning systems, *IEEE Sens. Lett.* 1 (3) (2017) 1–4.
- [15] A.B. Mackay, D.G. Smith, S.P. Magleby, B.D. Jensen, L.L. Howell, Metrics for evaluation and design of large-displacement linear-motion compliant mechanisms, *J. Mech. Des.* 134 (1) (2012) 011008.
- [16] G. Hao, H. Li, Nonlinear analytical modeling and characteristic analysis of a class of compound multibeam parallelogram mechanisms, *J. Mech. Robot* 7 (4) (2015) 041016.
- [17] R.M. Panas, J.B. Hopkins, Eliminating underconstraint in double parallelogram flexure mechanisms, *J. Mech. Des.* 137 (9) (2015) 092301.
- [18] R.V. Jones, Some uses of elasticity in instrument design, *J. Sci. Instrum.* 39 (5) (1962) 193–203.
- [19] D.M. Brouwer, A. Otten, J.B.C. Engelen, B. Krijnen, H.M.J.R. Soemers, Long-range elastic guidance mechanisms for electrostatic Comb-drive actuators, in: *Proceedings of the EUSPEN International Conference*, Delft, The Netherlands, 2010.
- [20] V.K. Venkiteswaran, H.J. Su, A three-spring pseudorigid-body model for soft joints with significant elongation effects, *J. Mech. Robot.* 8 (6) (2016) 061001.
- [21] S. Sood, *Analysis of Single Axis Flexure Bearings Approaching Ideal Bearing Characteristics* M.S. Thesis, University of Michigan, Ann Arbor, MI, August 2013.

- [22] Y. Li, J. Huang, H. Tang, A compliant parallel XY micromotion stage with complete kinematic decoupling, *IEEE Trans. Autom. Sci. Eng.* 9 (3) (2012) 538–553.
- [23] B. Zhang, S.A. Billings, Z.-Q. Lang, G.R. Tomlinson, Suppressing resonant vibrations using nonlinear springs and dampers, *J. Vib. Control* 15 (11) (2009) 1731–1744.
- [24] R. Ramlan, M.J. Brennan, B.R. Mace, I. Kovacic, Potential benefits of a non-linear stiffness in an energy harvesting device, *Nonlinear Dyn.* 59 (4) (2010) 545–558.
- [25] G. Hao, J. Yu, Y. Liu, Compliance synthesis of a class of planar compliant parallelogram mechanisms using the position space concept, *Proceedings of the 4th IEEE/IFToMM International conference on Reconfigurable Mechanisms and Robots*, 2018.